The 2020 eruption and the large lateral dike emplacement at Taal volcano, Philippines: Insights from radar satellite data

M.G Bato [1], P. Lundgren [1], V. Pinel [2], R. Solidum [3], A. Daag [3], and M. Cahulogan [3]

[1]Jet Propulsion Laboratory, California Institute of Technology, California, USA
[2]Univ. Grenoble Alpes, Univ. Savoie Mont Blanc, CNRS, IRD, IFSTTAR, ISTerre, Grenoble, France
[3]Philippine Institute of Volcanology and Seismology (PHIVOLCS), Department of Science and Technology (DOST), Quezon City, Philippines

Key Points:

- We present a comprehensive InSAR-based data, analyses, and models of Taal's pre- to post-eruptive state.
- During the eruptive crisis, Taal's magma reservoir lost 0.531 ± 0.004 km^3 of volume while a 0.643 ± 0.001 km^3 lateral dike was emplaced.
- Low-latency InSAR-derived products provided crucial and significant information to PHIVOLCS during the January 2020 eruptive event.

Corresponding author: M. Grace Bato, bato@jpl.nasa.gov

Abstract

On 12 January 2020, Taal volcano, Philippines, erupted after 43 years of repose, affecting more than 500,000 people. Using interferometric synthetic aperture radar (InSAR) data, we present the complete pre- to post-eruption analyses of the deformation of Taal. We find that: 1) prior to eruption, the volcano experienced long-term deflation followed by short-term inflation, reflecting depressurization-pressurization of its ~ 5 km depth magma reservoir; 2) during the eruption, the magma reservoir lost a volume of 0.531 ± 0.004 km^3 while a 0.643 ± 0.001 km^3 lateral dike was emplaced; and 3) post-eruption analyses reveal that the magma reservoir started recovery approximately 3 weeks after the main eruptive phase. We propose a conceptual analysis explaining the eruption and address why, despite the large volume of magma emplaced, the dike remained at depth. We also report the unique and significant contribution of InSAR data during the peak of the crisis.

Plain Language Summary

Taal volcano in the Philippines erupted on 12 January 2020. Here, we present the pre-, co-, and post-eruption data, model, and analyses using InSAR data acquired by various satellite systems. We find that: 1) prior to the eruption, the volcano experiences a sequence of long-term deflation followed by short-term inflation as result of the depressurization - pressurization of its ~ 5 km depth magma reservoir; 2) during the eruption, the magma reservoir lost a volume of 0.531 ± 0.004 km^3 while a 0.643 ± 0.001 km^3 lateral dike was emplaced; and 3) post-eruption analyses reveal that the magma reservoir is in recovery starting ~ 3 weeks after the main eruptive phase. We propose a conceptual analysis to explain the 2020 Taal eruption and the dike emplacement. We also report the unique and significant contribution of remote sensing data, particularly InSAR during the peak of the crisis.

1 Introduction

Taal volcano is a caldera located in southwestern Luzon island in the Philippines (Figure 1). It is one of the frequently erupting volcanoes in the country having at least 33 known historical eruptions between AD1572 and AD1977 (Delos Reyes et al., 2018). The volcano is part of the Macolod Corridor, a complex NE-SW trending 50-60 km-wide rift zone, characterized by active volcanism, crustal thinning, extensive faulting, and block rotation (Delos Reyes et al., 2018; Galgana et al., 2014; Pubellier et al., 2000; Wolfe & Self, 1983). Recent activities at Taal are limited to with the Volcano Island (VI), a 5 km wide, 311 m high resurgent dome with over 40 volcanic vents in the middle of Taal lake, with the largest being the Main Crater (Zlotnicki et al., 2018; Delos Reyes et al., 2018). Eruption dynamics of Taal are controlled by local tectonics, and magma reservoir-water interactions from external sources (e.g. rainwater and groundwater) that can result in different eruption styles and a wide range of explosivity (Zlotnicki et al., 2018; Delos Reyes et al., 2018; Pubellier et al., 2000).

On 12 January 2020, around 05:00 UTC, Taal volcano experienced a phreatic eruption spewing a column of steam-laden ash reaching ~ 15 km high and accompanied by frequent volcanic lightning as reported by the Philippine Institute of Volcanology and Seismology (PHIVOLCSa, 2000). The eruption transitioned to a phreato-/magmatic phase by 18:49 UTC as evidenced by weak lava fountaining in the Main Crater of VI (PHIVOLCSb, 2000; Martinez-Villegas, 2000). We refer to the 12 January event as the main co-eruptive event in this paper. After the main eruptive phase, Taals activity began to gradually wane and by 19 March 2020, PHIVOLCS downgraded the alert level to 1 indicating a low level of volcanic unrest (PHIVOLCSc, 2000). A total of 565,005 individuals were directly affected by this crisis with $\sim$\$69M worth of damage to infrastructure and agriculture reported (NDRRMC, 2000).

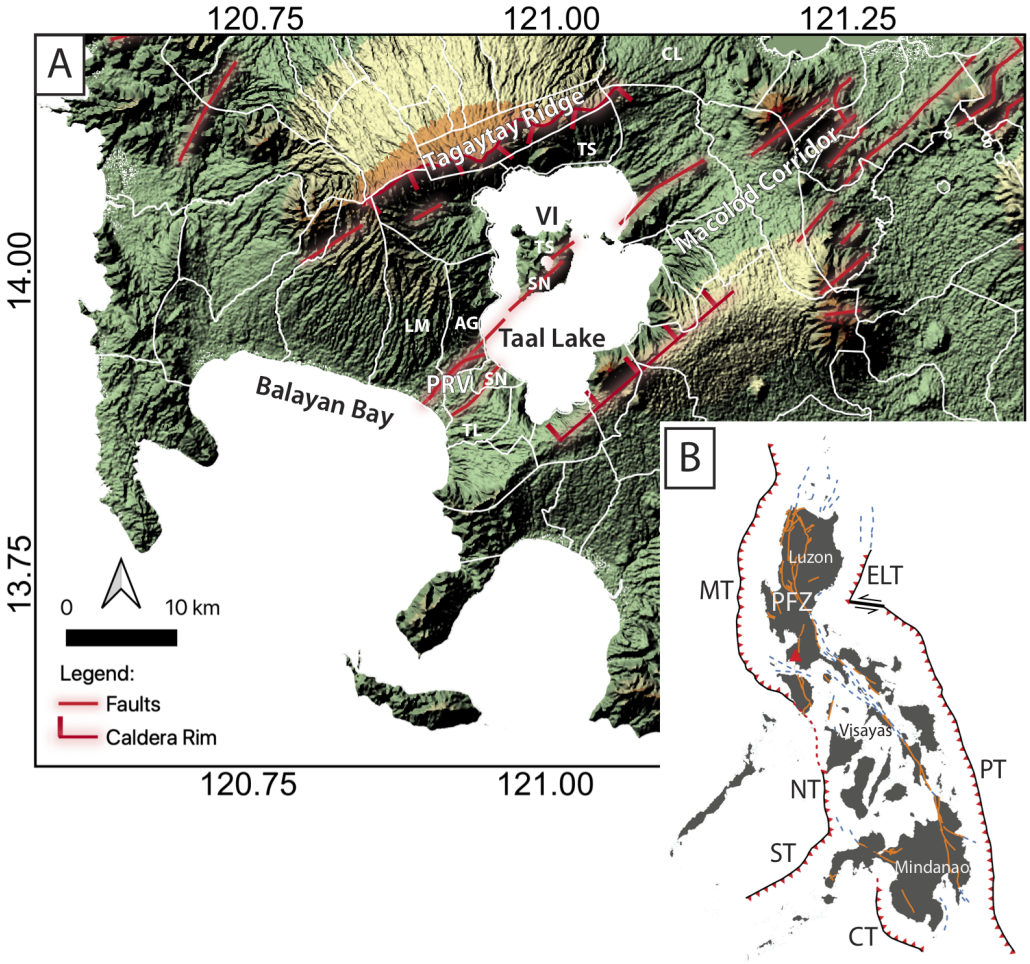

Figure 1. (A) Map showing Taal volcano and the local tectonic features in the vicinity including parts of the Macolod Corridor (modified after Delos Reyes et al. (2018); Pubellier et al. (2000)). VI: Volcano Island; PRV: Pansipit River Valley. White outlines are town boundaries. LM: Lemery; AG: Agoncillo; TL: Taal; SN: San Nicolas: TS: Talisay; CL: Calamba. (B) The Philippine archipelago and the major tectonics controlling the region. Two opposing subduction zones create the oblique convergence in the Philippines: to the west are the Manila-Negros-Sulu and Cotabato trenches, and to the east is the Philippine Trench. The result of this oblique plate motion is the Philippine Fault Zone which is a 1200-km long left-lateral strike-slip fault that traverses the archipelago from north to south (Aurelio, 2000). Orange solid lines are active faults and blue broken lines are offshore extension of the active faults. The red triangle is the location of Taal volcano. MT: Manila Trench, NT: Negros Trench, ST: Sulu Trench, ELT: East Luzon Trough, PFZ: Philippine Fault Zone, CT: Cotabato Trench, PT: Philippine Trench.

Here, we present the complete pre- to post-eruption analyses of the January 2020 Taal eruption and dike emplacement using interferometric synthetic aperture radar (InSAR) datasets. We discuss a conceptual analysis on what drove the 2020 eruption as well as explain why the dike remain emplaced at depth. We also report the significant contribution of InSAR data during the on-going crisis when most of the in-situ instruments were not operating.

2 Data and Methods

2.1 InSAR and time-series processing

2.1.1 Pre-eruptive dataset

We explore surface deformation using synthetic aperture radar (SAR) data from two systems: the Japan Aerospace Exploration Agency (JAXA) ALOS-2 satellite's PALSAR-2 L-band (23.8 cm wavelength) sensor and the Copernicus Sentinel-1A/B dual satellites's C-SAR C-band (5.5 cm wavelength) sensor operated by the European Space Agency (ESA). All the datasets were processed into differential interferograms of surface deformation projected into the radar line-of-sight (LOS) after correcting for Earth curvature and topographic effects.

The ALOS-2 SAR data were processed at the Jet Propulsion Laboratory (JPL) using the InSAR Scientific Computing Environment (ISCE) software (Rosen et al., 2018). The Sentinel 1A/B SAR data were processed through JPL's Advanced Rapid Imaging and Analysis (ARIA) Project based on nearest-neighbor pairing strategy, N=3. We compute the InSAR time-series for each track of the two satellite systems using the MintPy software (Yunjun et al., 2019). In addition, for comparison, a time-series was computed for the Sentinel-1 descending track (i.e. 5 May 2016-09 January 2020) using the New Small Baselines Subset (NSBAS) processing chain modified to allow TOPSAR data ingestion (Grandin, 2015; Doin et al., 2011).

2.1.2 Co-eruptive datasets

We utilized SAR data acquired by Sentinel 1A/B between 09 and 17 January 2020 covering the main eruptive event to produce the InSAR phase and pixel-offset maps using ISCE. The descending dataset captured the deformation from 09-15 January 2020, whereas the ascending dataset spans 11-17 January 2020. We derived the horizontal and vertical displacements following the method of Wright et al. (2004).

2.1.3 Post-eruptive datasets

We explore Sentinel-1 SAR data from 15 January to 27 June 2020 for both the descending and ascending orbits. The interferograms were processed using ISCE and we computed the post-eruptive time-series for both tracks using MintPy. We divided the time-series into two epochs (i.e. 15 January - 04 February and 2) 02 February - 27 June) based on the change in deformation trend within VI and derived the horizontal and vertical cumulative displacement maps following Wright et al. (2004).

2.2 Geodetic source modeling

2.2.1 Pre-eruptive modeling

We used the Caltech-JPL-developed AlTar v2.0 Bayesian inversion software. AlTar is based on the Cascading Adaptive Transitional Metropolis in Parallel method of Minson et al. (2013). To constrain the model, we utilized the Sentinel-1 and ALOS-2 velocity maps from the time-series inversion covering one year of the inflation event before

the eruption. We subsampled each dataset and computed the covariances by applying a model-based quadtree approach (Lohman & Simons, 2005) using a sill model.

We used the compound dislocation model (CDM) (Nikkhoo et al., 2017) implemented in AlTar to model the magmatic reservoir beneath Taal. The CDM model approximates an arbitrarily oriented and shaped ellipsoidal reservoir (from cigar to pancake). Overall, CDM has ten parameters: three for the locations (x, y, z), three for the semi-axes lengths (a, b, c), three for the rotations $(\omega_X, \omega_Y, \omega_Z)$, and a uniform opening, u. We also estimated the shifts in the InSAR data since InSAR measurements are relative measurements based on a reference point. In the end, we estimated 14 parameters. We extract the optimal parameter values by calculating for the maximum *a posteriori* probability (MAP) solutions.

2.2.2 Co-eruptive modeling

We follow the approach of Lundgren et al. (2013) to model the co-eruptive deformation source. The modeling occurred in two steps: (1) we solve for a deflating magma reservoir beneath Taal using a CDM and a simple planar tensile dislocation (dike) model with uniform opening, and (2) after we fixed the parameters of the CDM and the rectangular dislocation, we developed a distributed opening model to further constrain the dike dimensions and opening.

We use the Sentinel-1 InSAR ascending and descending cumulative LOS displacements and the descending range-offset maps for the co-eruptive modeling since these data provided better constraints on the initial activity of the dike. We down-sampled each dataset and calculated their covariances using a model-based quadtree approach (Lohman & Simons, 2005) given a dike model.

2.2.3 Post-eruptive modeling

We only modeled the deformation from 15 January to 04 February 2020 to track the further activity of the dike after the main eruptive phase using the Sentinel-1 ascending and descending cumulative LOS displacements. Following the steps in section 2.2.2, we first fixed the geometry and locations of the magma reservoir and the dike either by: ***Case 1)*** using the co-eruptive MAP solutions (Table S1) or ***Case 2)*** independently estimating for the dike parameters using MCMC (Table S1). Afterwards, we inferred for the closing of the reservoir and the distributed opening of the dike using the non-negative least squares method.

3 Crisis Response Story

During the peak of the eruption, most of the monitoring instruments installed on VI were either destroyed or temporarily stopped operating. SAR data delivered with low-latency were essential for determining the state of the volcano and in guiding the decision-making of PHIVOLCS. On 12 January, we initiated a crisis response by producing interferograms using 1) ALOS-2 descending SAR datasets spanning one year (i.e. 13 January 2019 to 12 January 2020) and 2) Sentinel-1 ascending SAR datasets covering 12 days prior to the eruption (i.e. 30 December 2019 to 11 January 2020) to determine if there was any pre-eruptive deformation detected by InSAR. The ALOS-2 descending interferogram (Figure 2A) which covered a longer duration has relatively good coherence over the entire area and showed roughly two fringes crossing VI ($\sim$ 24 cm of LOS surface deformation). The Sentinel-1 ascending interferogram (Figure 2B) has poor coherence particularly for vegetated areas and showed null to very small short-term deformation. Regions outside the European territory are typically imaged by the Sentinel-1 satellite every 12 days. To monitor the on-going volcanic crisis with low-latency, the International Disaster Charter was triggered and at the same time, we requested a 6-day repeat Sentinel-

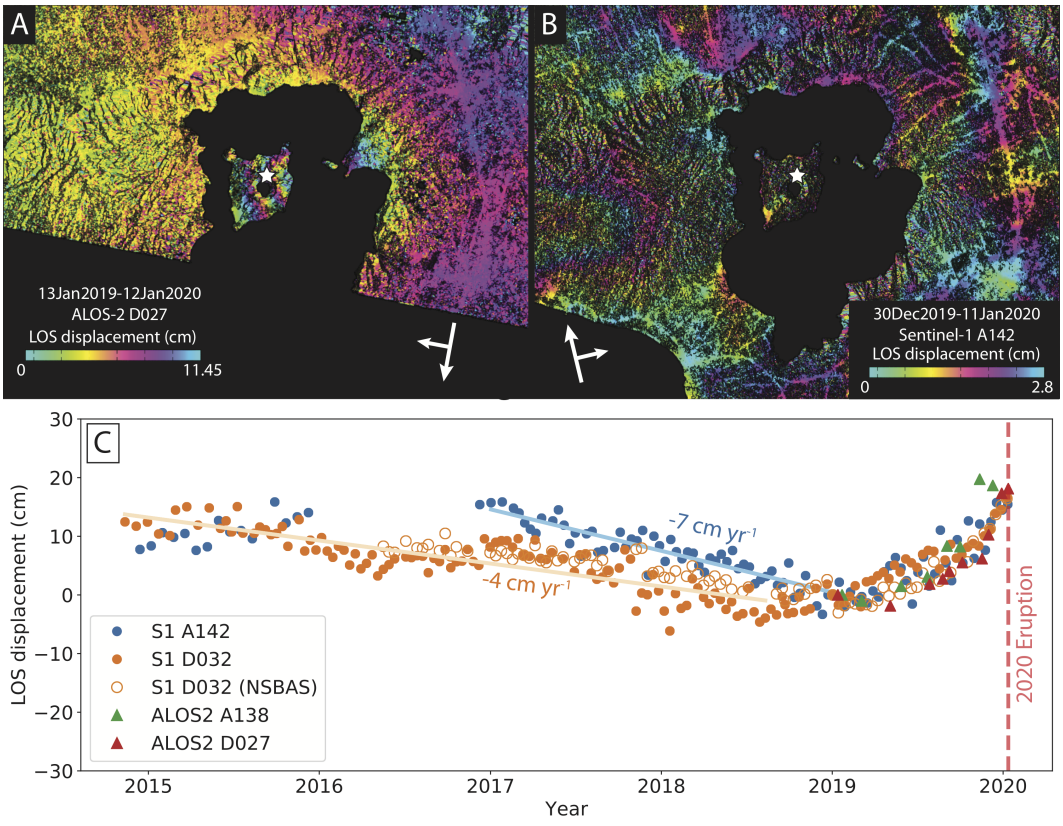

Figure 2. (A-B) Pre-eruptive interferograms of Taal produced using ALOS-2 L-band (A) and Sentinel-1 C-band (B) satellite dataset showing long- and short-term surface deformations, respectively. (C) Surface LOS displacement time-series measured at 14.0188° N, 121.0012° E (i.e. star symbol) from both the ascending and descending tracks of ALOS-2 and Sentinel-1 starting in late 2014 and leading up to the 12 January 2020 Taal eruption (dashed red line). For each time-series, we referenced the date to their respective first acquisitions in January 2019 (ALOS-2 A138: 22 January 2019; ALOS-2 D027: 13 January 2019; S1 A142: 04 January 2019; S1 D032: 02 January 2019) Blue dots: displacement time-series from Sentinel-1 ascending track 142. Orange dots: displacement time-series from Sentinel-1 descending track 032. Orange circles: displacement time-series from Sentinel-1 descending track 032 generated using the NSBAS processing chain. Note that the NSBAS-derived result is only shown here for comparison and was not used during the inversion. Green triangles: displacement time-series from ALOS-2 track ascending track A138. Red triangles: displacement time-series from ALOS-2 descending track 027. The light blue and light orange lines correspond to the negative displacement trend for the Sentinel-1 derived measurements.

1 acquisition from the European Space Agency (ESA), which operates Sentinel-1 for the Copernicus program of the European Commission. ESA granted the request until 22 February 2020.

On 15 January, after the descending SAR data became available in the Copernicus sci-hub repository (https://scihub.copernicus.eu/), we rapidly processed and directly communicated the first co-eruptive Sentinel-1 interferogram (Figure 3A) to PHIVOLCS through a messaging applicationjust in time for their science discussion and planning. The interferogram revealed dense fringes within VI and the Pansipit River Valley (PRV). However, due to the large deformation caused by the eruption, it was difficult to measure the ground displacements within these areas. The pixel-offset analysis (Figure 3C) enabled us to see through the regions that have significantly changed, however, with a lower accuracy compared to InSAR-derived phase measurements. We interpreted the signal from this first co-eruptive InSAR and pixel-offset maps as a result of the emplacement of a large dike and the deflation of a magma reservoir. This initial interpretation during the on-going crisis was further supported by the subsequent ascending interferogram and modeling (see Section 5). If a dike-fed eruption had occurred at that time, we could resolve the location to the vicinity of PRV, where the towns of Taal, Lemery, Agoncillo, and San Nicolas would have been directly affected. The information derived from low-latency InSAR imageries coupled with the recorded seismicity during the eruption were indeed unprecedented for the Philippines, enabling PHIVOLCS to continue monitoring the volcanic state. We continued providing InSAR data and analyses to PHIVOLCS as the eruption progressed until it had completely waned.

4 The pre-eruptive state, location, and geometry of the magma storage beneath Taal

The Sentinel-1 datasets stretch back from late 2014 until one day before Taals phreatic eruption. For both the Sentinel-1 tracks (Figure 2C), the time-series reveal a negative trend in the measured LOS displacement from 2014 until late 2018 before the rapid increase in displacement that precedes the 12 January 2020 eruption. This negative trend followed by a positive displacement trend has also been recorded through geodetic surveys conducted by PHIVOLCS (PHIVOLCS, 2019). The ALOS-2 time-series from both tracks started in late 2018 until a few hours before the eruption and thus only reveal the inflationary part of the deformation time-series.

From the inversion, we find a NE-SW striking ellipsoidal body located at ~ 5 km depth beneath the Main Crater of VI (Figure S1-S2). The estimated reservoir volume change was 0.045 ± 0.007 km^3 over the year prior to the eruption (Figure S3A). Seismic analysis (Kumagai et al., 2014) and geodetic studies of Taal volcano also showed a reservoir at similar depth and location, although with a spherical-shaped chamber (Morales-Rivera et al., 2019; Zlotnicki et al., 2018; Galgana et al., 2014; Bartel et al., 2003). Figure S2 gives the data, model and residual maps using the MAP values illustrating a good fit between the model inversion results and data.

5 Magma withdrawal and dike emplacement

From the co-eruptive InSAR phase (Figure 3A-3B) and pixel-offset (Figure 3C-3D) displacement maps, we derived the horizontal (Figure 3E) and vertical displacements (Figure 3F-3G). Two distinct signals emerged: 1) VI and the north and east portions of the Taal caldera experienced deflation of ~ 4 m, and 2) the SW region from VI towards Balayan Bay inflated ($\sim$ 1 m) and pulled apart ($\sim$ 2 m), with the center of the NE-SW trending rift located near the Pansipit river. In volcano geodesy studies, these signals are typical indications of magma withdrawal from a reservoir and magma emplacement through dike intrusion at depth.

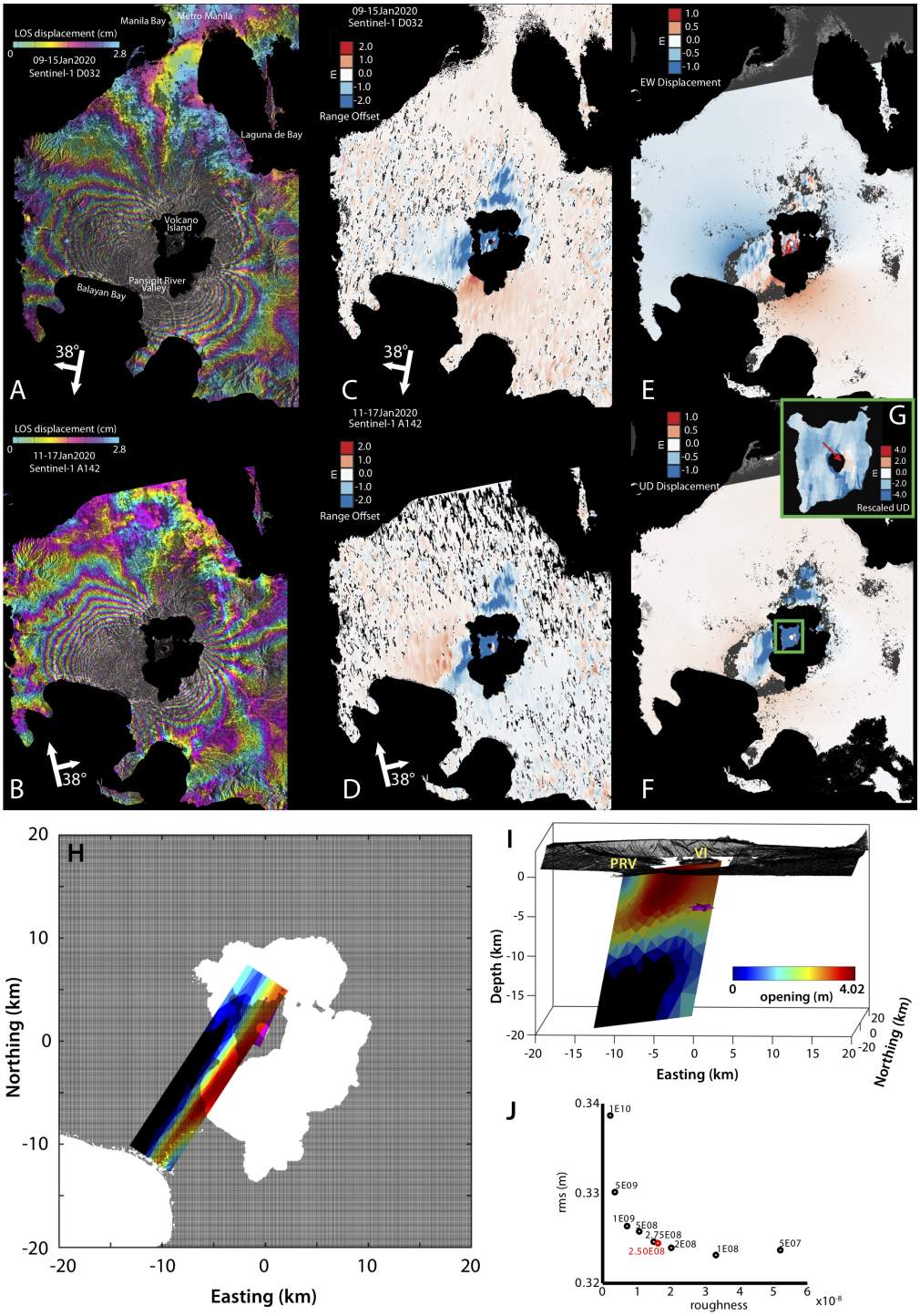

Figure 3. The co-eruptive datasets and model. (A-B) The InSAR phase and (C-D) range-offset displacement maps from Sentinel-1 descending and ascending tracks showing how much the ground moved as a result of the Taal eruption and dike emplacement. (E-F) Derived horizontal and vertical displacements from InSAR phase and range-offset maps. Note that areas covered by fringe aliasing in the InSAR maps are masked and are replaced by range-offset data. (G) Magnified view of the vertical displacement map to highlight the local subsidence within the island and the location of emplaced volcanic deposits (red arrow). (H) Map view and (I) 3D view of the CDM and distributed slip model. PRV: Pansipit River Valley; VI: Volcano Island. (J) Solution root-mean-square misfit vs. fault slip roughness as a function of the smoothing value used for the dike. The value in red text is the smoothing factor that we used for the co-eruptive model.

From the co-eruptive modeling, we find that the magma reservoir at $\sim 5-6$ km depth below VI lost an estimated volume of 0.531 ± 0.004 km^3 (Figure S3B; Figure S4), which is an order of magnitude larger than the accrued volume change of the reservoir the prior year. This indicates that only a small percentage of the magma withdrawn from the reservoir came from the short-term accumulation period. The model also revealed that a 21 km x 8 km, near-vertically dipping, NE-striking dike was intruded below the surface from VI extending southwestward toward Balayan Bay (Figure S5). NE-SW trending ground fissures that emerged in the municipalities of Agoncillo, Lemery, San Nicolas, Taal, and Talisay, matched the results of our dike model (PHIVOLCSd, 2000). We estimated that the volume of the dike is 0.643 ± 0.001 km^3 (Figure S3C) assuming a uniform slip opening. This is $1.2\times$ greater than the volume loss of the magma reservoir, implying that the volume difference may be due to additional deep source input or the effect of magma compressibility as a result of degassing (Rivalta & Segall, 2008). We calculated that if half of the dikes volume had erupted explosively, it might have yielded a volcano eruption index (VEI) 4 eruption (Newhall & Self, 1982).

The co-eruptive distributed slip model in Figure 3H-3I indicated strong opening below VI that extended southwestward toward PRV at < 10 km depth. Although the strongest opening is found beneath Taal Lake, it is unclear if the dike reached the bottom of the lake which has a maximum depth of 198 m (Castillo & Gonzales, 1976). Notice that the co-eruptive model also shows opening at around 15-20 km depth indicating that there may be a possible deep source feeding the shallow reservoir, although this can also represent the inability of the shallower portions of the model to fit far-field LOS displacements that may be dominated by sources of noise in the InSAR data. Figure S7 shows the co-eruptive data, model, and residual maps using the MAP values, illustrating a good fit between the model and the data.

Subsequent to the main eruptive phase, persistent surface deformation was still observed at Taal (Figure 4A-4D; Figure S8-S12). VI continued to deflate of up to 0.8 m until around 04 February (Figure 4A and 4C) before inflationary signals are detected (Figure 4B and 4D; Figure S8 and S10). Ground displacements are sustained around PRV toward Balayan Bay, with most of the significant deformation occurring almost simultaneous to the deflation of VI. We observed that the reservoir continued to lose volume (i.e. 0.0075 ± 0.0001 km^3, Figure S3D) while the dike further grew (i.e. 0.0557 ± 0.0004 km^3, Figure S3E) until 04 February.

The post-main eruptive phase distributed slip model between 15 January and 04 February shows weak opening (i.e. up to 41 cm) centered mostly above 10 km-depth beneath Taal lake (Figure 4E-4F). No further dike propagation is thus evidenced, although the resolution of the dike tip position is limited by the absence of information on the displacement field under the sea. The fit between the model and the data are reasonable (Figure S13) in the first order. Most of the residuals are probably due to 1) the change in the dike orientation as it propagates (i.e. shift to a more vertically-dipping dike, Figure S14-S17) and/or 2) some transient processes (i.e. local faulting events) that are not taken into account in the post-eruptive model.

Between 02 February and 27 June, InSAR time-series of Taal reveal that 1) the magma reservoir beneath VI is in recovery as evidenced by the inflation detected around the island, and 2) no significant surface deformation was detected in PRV and in the nearby areas (Figures S8-S12). The re-inflation and thus, the refilling of the magma reservoir is consistent with our co-eruptive model showing possible evidence of a shallow reservoir fed by a deeper source.

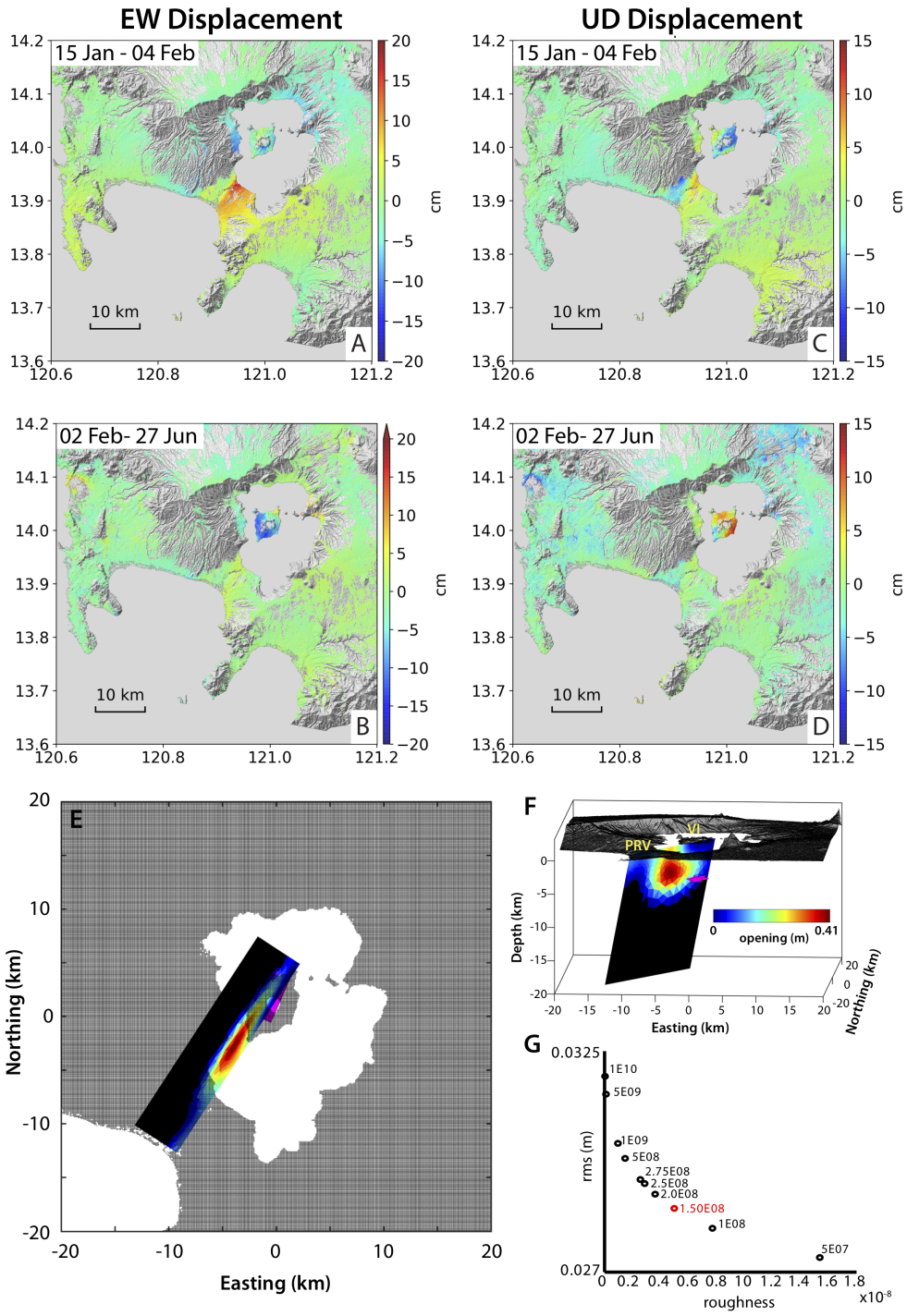

Figure 4. Post-eruptive datasets and model. Horizontal (A-B) and vertical displacement (C-D) maps derived from the descending and ascending cumulative displacements covering two periods: (A,C) 15 January-04 February and (B,D) 02 February to 27 June 2020. (A-B) Red means that the ground moved eastward, blue signifies that the ground moved westward. (C-D) Red means that the ground moved upward and blue represents downward movement. (E) Map view and (F) 3D view of the post-eruptive model covering 15 January-04 February 2020. For this model (i.e. post-eruptive model: Case 1), we fixed the geometries and locations of the CDM and the dike using the co-eruptive MAP results (see Table S1). (G) Solution root-mean-square misfit vs. fault slip roughness as a function of the smoothing value used for the dike. The value in red text is the smoothing factor that we used for the post-eruptive model.

6 Discussion

When a volcanic eruption occurs, we ask the obvious however difficult fundamental questions. *What drives the eruption? Why and when did the shallow magmatic storage became unstable and failed?* And for Taals specific case, *why did the magma favour lateral propagation and remain stalled at depth?*

Magma produced in the mantle is thought to rise in the form of dike or melt-pocket injections through cracks in the crust driven by its buoyancy relative to the surrounding crust. It can stall at depth once it loses buoyancy or cools and sometimes when it encounters a barrier. Magma may accumulate at shallower zones before erupting to the surface and form magma reservoirs through series of intrusions. The driving mechanism[s] that control[s] the timescale, migration and storage of magma at shallow depths remains poorly understood. Recently, a model whereby passive degassing causes decompression followed by rapid magma ascent and pressurization of the shallow reservoir has been proposed as a possible mechanism for eruption at volcanoes with hydraulically connected plumbing systems (Girona et al., 2014, 2015). In this model, degassing creates a pressure imbalance that promotes magma ascent from the deep to shallow magma reservoirs. Time-series of both the surface displacement data and the thermal warming of the volcanic edifice at Domuyo volcano in Argentina support a possible variation on this model (Lundgren et al., 2020).

The balance between vertical and lateral propagation is a key question central to many magmatic systems, occurring not only in rift zones, such as Krafla, Afar, and Bárdarbunga, but also at basaltic volcanoes such as Kīlauea, Ambrym, and Piton de la Fournaise. In these systems, a large volume of magma travels laterally, whether the eruptive sequence starts with an eruption in the central area, as observed at Piton de la Fournaise in 2007 (Froger et al., 2015) and Ambrym in 2018 (Shreve et al., 2019), or without eruption in the central part but deflation due to the lateral dike propagation and distal eruption as found for Bárdarbunga, 2015 (Sigmundsson et al., 2015) and Kīlauea, 2018 (Neal et al., 2019). However, there are also cases where lateral dike propagation does not feed an eruption (Wright et al., 2006; Sturkell et al., 2006), as in the case of Taals 2020 event.

The direction of magma propagation is mainly controlled by the local stress field and the magma driving pressure due to buoyancy and bottom magma influx, (Pinel et al., 2017) as well as local rheology (Urbani et al., 2018, 2017). Indeed, positive buoyancy will always favour magma ascent and in all models of lateral propagation (Urbani et al., 2017; Townsend et al., 2017; Heimisson et al., 2015; Grandin et al., 2012; Buck et al., 2006; Pinel & Jaupart, 2004; Einarsson et al., 1980), buoyancy should act against the direction of propagation, being controlled by the local stress field and/or the topography.

For Taals case, its shallow reservoir became unstable and ruptured due to a small magma input during the short-term accumulation period. The sudden magma input might have been induced by the depressurization resulting from the degassing of the shallow storage zone, consistent with the long-term deflation preceding the short-term inflation and gas emission records. CO_2 flux measurements of Taal volcano range from 500 to 4000 t/d during quiescence and were accompanied by large seismic activity (Zlotnicki et al., 2018; Arpa et al., 2013). In addition to this, thermal warming time-series of Taals edifice from satellite optical data analysis, a proxy to the ascent of hot gases from magma reservoirs (Girona et al. (2020), Girona personal communication), shows positive acceleration of the temperature change prior to seismic crises within the last decade.

As the magma reservoir accumulated pressure, it also interacted with the overlying hydrothermal system at approximately 2.5 km depth (Zlotnicki et al., 2018). The hydrothermal system may have been 1) heated, pressurized, and sealed or 2) destabilized due to the input of magma, either as small batches or through interaction with the

large dike, which triggered a phreatic event and led to the failure of the magma reservoir. Such interpretations are also consistent with geochemical analyses of Taal's hydrothermal system from 1991-2017 (Maussen et al., 2018). Zlotnicki et al. (2018) estimated that ~ 0.022 km^3 initial volume of eruptive products can be involved in a phreatic eruption due to the mechanically weak and mineralised materials in the northern part of VI as a result of the active fissures and geothermal field in the area that are stimulated by subsurface volcanic processes. This estimated initial volume is very close to the ~ 0.032 km^3 of erupted tephra in 12-13 January 2020 (Martinez-Villegas, 2000).

Most probably, the magmatic-phreatomagmatic eruption that occurred in VI was driven by an initial gas-rich phase which further decreased the remaining gas in the shallow storage zone. The orientation of the lateral dike is consistent with the pre-existing fault structures along the NE-SW-striking Macolod Corridor extensional zone, and appear to have played a significant role during the diking event by promoting the opening in the direction of the minimum compressive stress and the propagation along the maximum compressive stress (Delaney et al., 1986; Cotterell & Rice, 1980; Anderson, 1951). The fact that Taal's topography is very low could have also favored the deflection of the magma (Gaete et al., 2019; Corbi et al., 2015). Both the deflection of the magma path towards the edge of the caldera and the predominance of a lateral transport compared to the vertical one indicate that the magma buoyancy was reduced, probably due to the efficient gas loss at pre-eruptive and initial eruptive phases.

Although our model showed possible rupture in the lake between PRV and VI, there is no currently reported evidence of underwater lava flow emplacement and our datasets are restricted inland such that we do not have enough constraints beneath the water. Post-eruption bathymetric studies and geochemical analyses of Taal lake will provide more information and constraints. Interestingly, our models indicate that the dike migrated at deeper depths toward PRV and the post-eruptive dike growth was limited to a widening beneath Taal lake. Such observations are in agreement with dike propagation models controlled by local topography, thus inhibiting vertical propagation (Maccaferri et al., 2016).

Combining all these pieces of evidence, we conclude that the Taal 2020 volcanic crisis did not result in a catastrophic eruption, despite its history and potential of creating large and destructive events, simply because there was insufficient pressure to drive the magma upward and hence remain stalled at depth. Eruptions in the Main Crater and ground fissuring related to dike intrusions or fault adjustments were reported in the past (Delos Reyes et al., 2018). Although the 2020 crisis was not highly destructive, the past eruptions closest to this event were probably those in 1749 and 1911, which were categorized as VEI 3-4 events (Delos Reyes et al., 2018). Both eruptions were characterized by violent phreatomagmatic or plinian eruptions in the Main Crater while NE-SW-striking ground fissures appeared 1) at the northern part of the volcano reaching as far as Calamba (1749) or 2) from Lemery to Calamba (1911) (Delos Reyes et al., 2018).

7 Lessons learned

Taal volcano is one of the most closely monitored active volcanoes in the world consisting of a multi-parametric network of ground instruments. In terms of satellite-based monitoring, this is the first time that comprehensive and well-documented InSAR-derived displacement maps, time-series analyses, and deformation modeling of Taals pre-, co-, and post-eruptive state are presented.

On one hand, the pre-eruptive InSAR time-series revealed the inflation during the year preceding the January 2020 eruption. Although this inflation has also been detected by the geodetic network of Taal, InSAR provided the complementary spatial information. We obtained the precise geometry, location, and source strength of the magma reser-

voir beneath VI which are helpful information when characterizing the potential magnitude of an impending eruption. On the other hand, the co-eruptive interferogram rapidly showed the emplacement of the large dike allowing us to constrain the possible location of a dike-fed eruption had it occurred at that time and to immediately estimate the maximum VEI, which are important information for crisis management.

Satellite data will never replace in-situ observations, however, they will provide complementary and significant information with unprecedented spatial coverage. Indeed, multiparametric datasets that are comprised of ground- and satellite-based measurements should be used in monitoring volcanoes to get a full perspective of the volcanic state and to obtain insights into poorly known volcanic processes.

The launch of the Sentinel-1 satellites in 2014 and 2016 has greatly improved InSAR science and applications, particularly, in the monitoring of crustal deformation, allowing broad access to free and low-latency SAR data. Taals recent crisis benefited a lot from Sentinel-1 and the continuous and real-time delivery of processed data, analyses, and models that were crucial and useful for the observatory when most ground instruments were no longer available. During the eruption, the biggest challenge that we encountered was related to how accurate and correct are the low-latency preliminary analyses and models that we provided to PHIVOLCS given the lack of prior InSAR baseline observations for Taal. Fortunately, although the results that we report in this manuscript required extensive reprocessing and utilization of larger datasets and tools, our analyses remained consistent with those delivered to the observatory during the height of the crisis and the overall behavior of the volcano also corroborated our results. Despite the non-availability of other co-eruptive in-situ data, actual surface deformation observed in the field such as the emergence of ground fissures and the occurrence of subsidence and uplift in the coastal lake regions based on available field photographs cross-validated our analyses and interpretations. We, therefore, highlight the need and encourage volcano observatories globally to include remote sensing data like InSAR as a major component in their regular monitoring of active volcanoes, particularly now that 1) the data are becoming more open, and 2) satellite system acquisitions are getting more advanced and suitable for highly-vegetated, and tropical regions. Indeed, with greater access comes a need for scientific responsibility, and thus the greater exploitation of satellite data will require scientists and experts who have the skill and the access to these products and tools to consider their social responsibility and to practice professional conduct (Newhall et al., 1999) especially during an on-going crisis. Volcanoes are highly nonlinear and unpredictable, any perturbation in the state of the system can lead to a wide range of scenarios. With the upcoming launch of advanced satellite systems that promise to deliver global and open-access products, misinterpretations delivered across all media platforms may arise and we need a collective effort to address them (Poland et al., 2019).

Acknowledgments

We thank Hook Hua, Lan Dang, and David Bekaert for activating and managing the ARIA Project Sentinel-1A/B SAR interferogram generation based on European Commission Copernicus Sentinel-1 satellite SAR data products courtesy of the European Space Agency. All the ARIA-produced interferograms used in this study are accessible via https://aria-products.jpl.nasa.gov/. We thank the Japan Aerospace Exploration Agency (JAXA) for providing ALOS-2 PALSAR-2 SAR L1.1 (SLC) data through RA6 Proposal P3024002 (PI Lundgren) used in the analyses; original L1.1 products JAXA 2019-2020. We are also grateful to Chris Newhall and Eric Fielding for the helpful discussions during the peak of the eruption, as well as to Társilo Girona for the thermal warming time-series. Part of this research was carried out at the Jet Propulsion Laboratory, California Institute of Technology, under a contract with the National Aeronautics and Space Administration (grant 281945.02.47.04.51). AlTar software development and modeling supported through the JPL R&TD program (project number 01STCR- R.18.245.034). V. Pinel ac-

knowledges support through the MagmaPropagator project (contract ANR-18-CE92-0037-01).

References

Anderson, E. M. (1951). *The dynamics of faulting and dyke formation with applications to Britain*. Oliver and Boyd.

Arpa, M., Hernández, P., Padrón, E., Reniva, P., Padilla, G., Bariso, E., ... others (2013). Geochemical evidence of magma intrusion at Taal volcano, Philippines, in 2010-2011 from diffuse carbon dioxide emissions. *Bull Volcanol*, *75*, 747.

Aurelio, M. A. (2000). Shear partitioning in the Philippines: constraints from Philippine Fault and global positioning system data. *Island Arc*, *9*(4), 584–597.

Bartel, B. A., Hamburger, M. W., Meertens, C. M., Lowry, A. R., & Corpuz, E. (2003). Dynamics of active magmatic and hydrothermal systems at Taal Volcano, Philippines, from continuous GPS measurements. *Journal of Geophysical Research: Solid Earth*, *108*(B10).

Buck, W. R., Einarsson, P., & Brandsdóttir, B. (2006). Tectonic stress and magma chamber size as controls on dike propagation: Constraints from the 1975-1984 Krafla rifting episode. *Journal of Geophysical Research: Solid Earth*, *111*(B12).

Castillo, B., & Gonzales, C. (1976). Hydrology of Taal Lake. *Fish Res J Philipp*, *1*(2), 62–75.

Corbi, F., Rivalta, E., Pinel, V., Maccaferri, F., Bagnardi, M., & Acocella, V. (2015). How caldera collapse shapes the shallow emplacement and transfer of magma in active volcanoes. *Earth and Planetary Science Letters*, *431*, 287–293.

Cotterell, B., & Rice, J. (1980). Slightly curved or kinked cracks. *International journal of fracture*, *16*(2), 155–169.

Delaney, P. T., Pollard, D. D., Ziony, J. I., & McKee, E. H. (1986). Field relations between dikes and joints: emplacement processes and paleostress analysis. *Journal of Geophysical Research: Solid Earth*, *91*(B5), 4920–4938.

Delos Reyes, P. J., Bornas, M. A. V., Dominey-Howes, D., Pidlaoan, A. C., Magill, C. R., & Solidum Jr, R. U. (2018). A synthesis and review of historical eruptions at Taal Volcano, Southern Luzon, Philippines. *Earth-science reviews*, *177*, 565–588.

Doin, M.-P., Guillaso, S., Jolivet, R., Lasserre, C., Lodge, F., Ducret, G., & Grandin, R. (2011). Presentation of the small baseline NSBAS processing chain on a case example: the Etna deformation monitoring from 2003 to 2010 using Envisat data. In *Proceedings of the fringe symposium* (pp. 3434–3437).

Einarsson, P., Brandsdóttir, B., et al. (1980). Seismological evidence for lateral magma intrusion during the July 1978 deflation of the Krafla volcano in NE-Iceland. *Journal of Geophysics— IF 32.18*, *47*(1), 160–165.

Froger, J.-L., Famin, V., Cayol, V., Augier, A., Michon, L., & Lénat, J.-F. (2015). Time-dependent displacements during and after the April 2007 eruption of Piton de la Fournaise, revealed by interferometric data. *Journal of Volcanology and Geothermal Research*, *296*, 55–68.

Gaete, A., Kavanagh, J. L., Rivalta, E., Hazim, S. H., Walter, T. R., & Dennis, D. J. (2019). The impact of unloading stresses on post-caldera magma intrusions. *Earth and Planetary Science Letters*, *508*, 109–121.

Galgana, G. A., Newman, A. V., Hamburger, M. W., & Solidum, R. U. (2014). Geodetic observations and modeling of time-varying deformation at Taal Volcano, Philippines. *Journal of volcanology and geothermal research*, *271*, 11–23.

Girona, T., Costa, F., Newhall, C., & Taisne, B. (2014). On depressurization of volcanic magma reservoirs by passive degassing. *Journal of Geophysical Research: Solid Earth*, *119*(12), 8667–8687.

Girona, T., Costa, F., & Schubert, G. (2015). Degassing during quiescence as a trigger of magma ascent and volcanic eruptions. *Scientific reports*, *5*, 18212.

Girona, T., Realmuto, V., & Lundgren, P. (2020). Volcanoes get warm for years prior to eruption.

Grandin, R. (2015). Interferometric processing of SLC Sentinel-1 TOPS data..

Grandin, R., Socquet, A., Doubre, C., Jacques, E., & King, G. C. (2012). Elastic thickness control of lateral dyke intrusion at mid-ocean ridges. *Earth and Planetary Science Letters*, *319*, 83–95.

Heimisson, E. R., Hooper, A., & Sigmundsson, F. (2015). Forecasting the path of a laterally propagating dike. *Journal of Geophysical Research: Solid Earth*, *120*(12), 8774–8792.

Kumagai, H., Lacson Jr, R., Maeda, Y., Figueroa, M. S., & Yamashina, T. (2014). Shallow S wave attenuation and actively degassing magma beneath Taal Volcano, Philippines. *Geophysical Research Letters*, *41*(19), 6681–6688.

Lohman, R. B., & Simons, M. (2005). Some thoughts on the use of InSAR data to constrain models of surface deformation: Noise structure and data downsampling. *Geochemistry, Geophysics, Geosystems*, *6*(1).

Lundgren, P., Girona, T., Bato, M. G., Realmuto, V. J., Samsonov, S., Cardona, C., ... Aivazis, M. (2020). The dynamics of large silicic systems from satellite remote sensing observations: the intriguing case of Domuyo volcano, Argentina. *Scientific Reports*, *10*(1), 1–15.

Lundgren, P., Poland, M., Miklius, A., Orr, T., Yun, S.-H., Fielding, E., ... others (2013). Evolution of dike opening during the March 2011 Kamoamoa fissure eruption, Kīlauea Volcano, Hawaii. *Journal of Geophysical Research: Solid Earth*, *118*(3), 897–914.

Maccaferri, F., Rivalta, E., Passarelli, L., & Aoki, Y. (2016). On the mechanisms governing dike arrest: Insight from the 2000 Miyakejima dike injection. *Earth and Planetary Science Letters*, *434*, 64–74.

Martinez-Villegas, M. (2000). *Volcano Risk Communication in the Philippines:Challenges, Lessons and Opportunities Taal Volcano 2020.* Retrieved from `https://drive.google.com/file/d/1sUrKHfObZKDBA8y1sDlNr9_CcqPORSWB`

Maussen, K., Villacorte, E., Rebadulla, R. R., Maximo, R. P., Debaille, V., Bornas, M. A., & Bernard, A. (2018). Geochemical characterisation of Taal volcano-hydrothermal system and temporal evolution during continued phases of unrest (1991–2017). *Journal of Volcanology and Geothermal Research*, *352*, 38–54.

Minson, S., Simons, M., & Beck, J. (2013). Bayesian inversion for finite fault earthquake source models ITheory and algorithm. *Geophysical Journal International*, *194*(3), 1701–1726.

Morales-Rivera, A., Amelung, F., Albino, F., & Gregg, P. (2019). Impact of crustal rheology on temperature-dependent viscoelastic models of volcano deformation: Application to Taal Volcano, Philippines. *Journal of Geophysical Research: Solid Earth*, *124*(1), 978–994.

NDRRMC. (2000). *Situational Report No. 74 re Taal Volcano Eruption.* Retrieved from `https://reliefweb.int/sites/reliefweb.int/files/resources/SitRep_No_74_re_Taal_Volcano_Eruption_issued_on_13_Feb_2020_6AM.pdf`

Neal, C. A., Brantley, S., Antolik, L., Babb, J., Burgess, M., Calles, K., ... others (2019). The 2018 rift eruption and summit collapse of Kīlauea Volcano. *Science*, *363*(6425), 367–374.

Newhall, C., Aramaki, S., Barberi, F., Blong, R., Calavache, M., Cheminee, J., ... others (1999). International Association of Volcanology and Chemistry (IAVCEI) Subcommittee for Crisis Protocols-Professional conduct of scientists during volcanic crises. *Bull Volcanol*, *60*, 323–34.

Newhall, C., & Self, S. (1982). The volcanic explosivity index (VEI) an estimate of explosive magnitude for historical volcanism. *Journal of Geophysical Research:*

Oceans, *87*(C2), 1231–1238.

Nikkhoo, M., Walter, T. R., Lundgren, P. R., & Prats-Iraola, P. (2017). Compound dislocation models (CDMs) for volcano deformation analyses. *Geophysical Journal International*.

PHIVOLCS. (2019). *Taal volcano bulletin 28 march 2019 9:15 am.* Retrieved from https://www.phivolcs.dost.gov.ph/index.php/taal-volcano-bulletin-menu/8117-taal-volcano-bulletin-28-march-2019-9-15-am-2

PHIVOLCSa. (2000). *Taal volcano bulletin 12 january 2020 07:30 pm.* Retrieved from https://www.phivolcs.dost.gov.ph/index.php/taal-volcano-bulletin-menu/9620-taal-volcano-bulletin-12-january-2020-07-30-pm

PHIVOLCSb. (2000). *Taal volcano bulletin 13 january 2020 8:00 a.m.* Retrieved from https://www.phivolcs.dost.gov.ph/index.php/taal-volcano-bulletin-menu/9625-taal-volcano-bulletin-13-january-2020-8-00-a-m

PHIVOLCSc. (2000). *Taal volcano bulletin: 19 march 2020 08:00 am.* Retrieved from https://www.phivolcs.dost.gov.ph/index.php/taal-volcano-bulletin-menu/9872-taal-volcano-bulletin-19-march-2020-08-00-am

PHIVOLCSd. (2000). *General location of fissures related to the january 2020 taal volcano eruptive activity.* Retrieved from https://www.phivolcs.dost.gov.ph/index.php/news/9662-general-location-of-fissures-related-to-the-january-2020-taal-volcano-eruptive-activity

Pinel, V., Carrara, A., Maccaferri, F., Rivalta, E., & Corbi, F. (2017). A two-step model for dynamical dike propagation in two dimensions: Application to the July 2001 Etna eruption. *Journal of Geophysical Research: Solid Earth*, *122*(2), 1107–1125.

Pinel, V., & Jaupart, C. (2004). Magma storage and horizontal dyke injection beneath a volcanic edifice. *Earth and Planetary Science Letters*, *221*(1-4), 245–262.

Poland, M. P., Pritchard, M. E., & Ebmeier, S. K. (2019). Low-latency remote sensing data in volcanology: justification, application, and communication. *AGUFM*, *2019*, IN51B–02.

Pubellier, M., Garcia, F., Loevenbruck, A., & Chorowicz, J. (2000). Recent deformation at the junction between the North Luzon block and the Central Philippines from ERS-1 Images. *Island Arc*, *9*(4), 598–610.

Rivalta, E., & Segall, P. (2008). Magma compressibility and the missing source for some dike intrusions. *Geophysical Research Letters*, *35*(4).

Rosen, P. A., Gurrola, E. M., Agram, P., Cohen, J., Lavalle, M., Riel, B., ... Buckley, S. M. (2018). The InSAR Scientific Computing Environment 3.0: A Flexible Framework for NISAR Operational and User-Led Science Processing. In *IGARSS 2018-2018 IEEE International Geoscience and Remote Sensing Symposium* (pp. 4897–4900).

Shreve, T., Grandin, R., Boichu, M., Garaebiti, E., Moussallam, Y., Ballu, V., ... others (2019). From prodigious volcanic degassing to caldera subsidence and quiescence at Ambrym (Vanuatu): the influence of regional tectonics. *Scientific reports*, *9*(1), 1–13.

Sigmundsson, F., Hooper, A., Hreinsdóttir, S., Vogfjörd, K. S., Ófeigsson, B. G., Heimisson, E. R., ... others (2015). Segmented lateral dyke growth in a rifting event at Bárdarbunga volcanic system, Iceland. *Nature*, *517*(7533), 191–195.

Sturkell, E., Einarsson, P., Sigmundsson, F., Geirsson, H., Olafsson, H., Pedersen, R., ... Stefánsson, R. (2006). Volcano geodesy and magma dynamics in Iceland. *Journal of Volcanology and Geothermal Research*, *150*(1-3), 14–34.

Townsend, M. R., Pollard, D. D., & Smith, R. P. (2017). Mechanical models for dikes: a third school of thought. *Tectonophysics*, *703*, 98–118.

Urbani, S., Acocella, V., & Rivalta, E. (2018). What drives the lateral versus verti-

cal propagation of dikes? Insights from analogue models. *Journal of Geophysical Research: Solid Earth*, *123*(5), 3680–3697.

Urbani, S., Acocella, V., Rivalta, E., & Corbi, F. (2017). Propagation and arrest of dikes under topography: Models applied to the 2014 Bárdarbunga (Iceland) rifting event. *Geophysical Research Letters*, *44*(13), 6692–6701.

Wolfe, J. A., & Self, S. (1983). Structural lineaments and Neogene volcanism in southwestern Luzon. *GMS*, *27*, 157–172.

Wright, T. J., Ebinger, C., Biggs, J., Ayele, A., Yirgu, G., Keir, D., & Stork, A. (2006). Magma-maintained rift segmentation at continental rupture in the 2005 Afar dyking episode. *Nature*, *442*(7100), 291–294.

Wright, T. J., Parsons, B. E., & Lu, Z. (2004). Toward mapping surface deformation in three dimensions using InSAR. *Geophysical Research Letters*, *31*(1).

Yunjun, Z., Fattahi, H., & Amelung, F. (2019). Small baseline InSAR time series analysis: Unwrapping error correction and noise reduction. *Computers & Geosciences*, *133*, 104331.

Zlotnicki, J., Sasai, Y., Johnston, M., Fauquet, F., Villacorte, E., & Cordon, J. (2018). The 2010 seismovolcanic crisis at Taal volcano (Philippines). *Earth, Planets and Space*, *70*(1), 1–23.